ROYAL SOCIETY
OF CHEMISTRY

PAPER

Check for updates

Nanostructured core–shell metal borides–oxides as highly efficient electrocatalysts for photoelectrochemical water oxidation†

Can Lu,[a] Palani R. Jothi, [ID][b] Thomas Thersleff,[c] Tetyana M. Budnyak, [ID][c]
Anna Rokicinska, [ID][d] Kunio Yubuta, [ID][e] Richard Dronskowski, [ID][a,f]
Piotr Kuśtrowski, [ID][d] Boniface P. T. Fokwa [ID] *[b] and Adam Slabon [ID] *[c]

Oxygen evolution reaction (OER) catalysts are critical components of photoanodes for photoelectrochemical (PEC) water oxidation. Herein, nanostructured metal boride MB (M = Co, Fe) electrocatalysts, which have been synthesized by a $Sn/SnCl_2$ redox assisted solid-state method, were integrated with WO_3 thin films to build heterojunction photoanodes. As-obtained MB modified WO_3 photoanodes exhibit enhanced charge carrier transport, amended separation of photogenerated electrons and holes, prolonged hole lifetime and increased charge carrier density. Surface modification of CoB and FeB significantly enhances the photocurrent density of WO_3 photoanodes from 0.53 to 0.83 and 0.85 mA cm^{-2}, respectively, in transient chronoamperometry (CA) at 1.23 V *vs.* RHE (V_{RHE}) under interrupted illumination in 0.1 M Na_2SO_4 electrolyte (pH 7), corresponding to an increase of 1.6 relative to pristine WO_3. In contrast, the pristine MB thin film electrodes do not produce noticeable photocurrent during water oxidation. The metal boride catalysts transform *in situ* to a core–shell structure with a metal boride core and a metal oxide (MO, M = Co, Fe) surface layer. When coupled to WO_3 thin films, the $CoB@CoO_x$ nanostructures exhibit a higher catalytic enhancement than corresponding pure cobalt borate ($Co-B_i$) and cobalt hydroxide ($Co(OH)_x$) electrocatalysts. Our results emphasize the role of the semiconductor–electrocatalyst interface for photoelectrodes and their high dependency on materials combination.

Introduction

Due to the rising global energy demand and corresponding environment concerns becoming a public focus, the production of environment-neutral fuels has been considered highly important.[1] Among the potential candidates, hydrogen

[a]*Institute of Inorganic Chemistry, RWTH Aachen University, Landoltweg 1, D-52056 Aachen, Germany*
[b]*Department of Chemistry and Center for Catalysis, University of California, Riverside, 92507 California, USA. E-mail: bfokwa@ucr.edu*
[c]*Department of Materials and Environmental Chemistry, Stockholm University, Svante Arrhenius väg 16 C, 10691 Stockholm, Sweden. E-mail: adam.slabon@mmk.su.se*
[d]*Faculty of Chemistry, Jagiellonian University, Gronostajowa 2, 30-387 Krakow, Poland*
[e]*Institute for Materials Research, Tohoku University, Katahira 2-1-1, Sendai 980-8577, Japan*
[f]*Hoffmann Institute of Advanced Materials, Shenzhen Polytechnic, Liuxian Blvd 7098, 518055 Shenzhen, China*
†Electronic supplementary information (ESI) available: Experimental section, supplemental figures, table and corresponding illustration. See DOI: 10.1039/c9nr09818f

has emerged to be one of the most promising energy carriers possessing superiorities such as high energy density and abundancy.[2,3] PEC water splitting is considered as a sustainable solution to directly produce hydrogen from water using solar fuel.[4,5] To date, significant improvement has been achieved for photocathodes; profiting highly from the experiences in industrial semiconductor production technology such as solar cell development.[6,7] Nevertheless, water oxidation involving the transfer of four electrons is demanding with respect to kinetics and stability, thus limiting the PEC water-splitting efficiency.[8,9] Consequently, it is crucial to develop highly active, stable and low-cost photoanodes to achieve commercialization of PEC technology in the future.

A broad variety of n-type semiconductors have been employed as photoabsorbers in photoanode-driven systems, including TiO_2,[10] $BiVO_4$,[11] $CuWO_4$,[12] and WO_3.[13] Due to the low catalytic activity of the semiconductor surface, it is essential to modify the light-absorber with electrocatalysts.[11,14] Although this strategy to improve current densities of thin film photoanodes is generally accepted, the influence of the semiconductor–electrocatalyst interface on the PEC OER cannot be predicted directly.[15] Only recently, metal boride catalysts have

shown excellent electrochemical catalytic performances due to their fast kinetics and superior stability, stemming from the synergistic effect of *in situ* formed thin oxide, hydroxide or oxyhydroxide layer and boride core.[3,16,17] A Ni-B@NiO$_x$H catalyst supported on nickel foam showed for instance 20 mA cm^{-2} at 0.28 V overpotential in 1.0 M KOH, which surpassed the activity of most previously reported nonprecious electrocatalysts for OER.[18] Within the core–shell catalysts, the surface shell functions as catalytic sites while the inner core facilitates charge transfer.[16,17,19]

However, to the best of our knowledge, there are only two reports on integrating metal borides as catalysts with semiconductors for water oxidation.[20,21] Dang *et al.* deposited NiB on a BiVO$_4$ photoanode to obtain improved charge carrier mobility and pronounced band bending was achieved, which led to a 100 mV cathodic shift of onset potential and boosted the photocurrent density to 3.47 mA cm^{-2} at 1.23 V$_{RHE}$, corresponding to 2.2-fold enhancement.[20] An *in situ* fabricated Fe$_2$O$_3$/FeB photoanode by Liao *et al.* doubled the photocurrent density at 1.23 V$_{RHE}$ relative to the pristine hematite, taking the advantages of ameliorated charge carrier separation and reduced charge transfer resistance.[21] These trials revealed the feasibility of utilizing metal borides as effective electrocatalysts to boost the PEC OER.

Conventionally, nanostructured metal boride catalysts are synthesized by the chemical reduction of metal salt precursors with NaBH$_4$.[3,22] An additional annealing treatment is usually necessary if crystalline structures need to be obtained.[16] From the practical application perspective for this kind of catalysts, more simple, cost-efficient, high-yield synthetic routes are preferred, for amenable mass production while enabling sufficient active sites.

We synthesized nanostructured CoB and FeB by a Sn/SnCl$_2$ redox assisted solid-state method with simple, highly efficient and large-scale amenable advantages.[23,24] These CoB nanosheets and FeB nanoplates were evaluated for the first time as PEC water oxidation catalysts to modify hydrothermally grown WO$_3$ thin films on fluorine doped tin oxide (FTO) glass. Mechanistic investigation demonstrated that the augmented water oxidation property originates from the synergetic effects through coupling WO$_3$ with *in situ* formed core–shell MB@MO.

Experimental

Photoanodes fabrication

The crystalline MB catalysts were prepared by a Sn/SnCl$_2$ redox assisted solid-state method.[23] WO$_3$ thin films were hydrothermally grown on FTO substrate followed by additional thermal treatment.[25] The MB-modified WO$_3$/MB thin film photoelectrodes were fabricated *via* drop-casting. For the comparison of the heterojunction WO$_3$/MB photoanodes, we synthesized catalysts such as Co-B$_i$ and Co(OH)$_x$.[26,27] These catalysts were deposited identically on WO$_3$ thin film. The exact experimental details are provided in the ESI.†

Characterization

The crystal structures of all samples were characterized by a powder X-ray diffractometer (PXRD, STOE STADI-P) with Cu K$_{\alpha 1}$ radiation in transmission mode. Surface morphology was characterized using a scanning electron microscope (SEM, Leo Supra 35VP SMT, Zeiss). High-resolution transmission electron microscopy (HRTEM) observation and selected area electron diffraction (SAED) characterization were conducted on a 200 kV electron microscope (TOPCON EM-002B). Electron energy-loss spectrum (EELS) was obtained in STEM mode from a Themis Z TEM (Thermo Fisher). The optical properties were characterized using a UV-vis spectrophotometer (UV-2600, Shimadzu). X-ray photoelectron spectroscopy (XPS) spectra were recorded using a hemispherical VG SCIENTA R3000 analyzer with a monochromatized aluminum source Al K$_\alpha$ (E = 1486.6 eV) at constant pass energy of 100 eV. The binding energies were referenced to the Au 4f core level (E_b = 84.0 eV) and the fitting of high-resolution spectra was obtained through the Casa XPS software.

Photoelectrochemical measurements

The PEC measurements were conducted in a three-electrode system under simulated Air Mass 1.5 Global solar light irradiation (AM 1.5G, 100 mW cm^{-2}, class-AAA 94023A, Newport) with the fabricated electrodes as the working electrodes, a platinum electrode as the counter electrode and a 1 M Ag/AgCl electrode as reference electrode. All measurements were conducted under back-side illumination and the measured potentials were adjusted to V$_{RHE}$ using the Nernstian relation ($E_{RHE} = E^0_{Ag/AgCl} + 0.059$ V × pH + $E_{Ag/AgCl}$). The electrolyte used was 0.1 M Na$_2$SO$_4$ aqueous solution with or without 50 mM Na$_2$SO$_3$ as holes scavenger (pH ≈ 7).

The linear sweep voltammetry (LSV) with a scan rate of 10 mV s^{-1} and chronoamperometry (CA) at a constant bias of 1.23 V$_{RHE}$ were performed with a potentiostat (PalmSens4, PalmSens BV). The electrochemical impedance spectra (EIS) were recorded under AM 1.5G irradiation in the range of 0.02 Hz to 20 kHz, with an AC voltage amplitude of 5 mV at a DC bias of 1 V$_{RHE}$. Mott–Schottky characterizations were carried out with an amplitude of 10 mV and frequency of 10 Hz under AM 1.5G illumination. Open circuit voltage (OCV) decay measurements were performed in Ar atmosphere and AM 1.5G light illumination was initiated once the OCV was stabilized in dark.

Results and discussion

Structural characterization

The synthesized WO$_3$ thin film can be assigned to the single, highly crystalline monoclinic phase (JCPDS no. 83-0951) observed in the PXRD patterns (Fig. S1†). The PXRD patterns of CoB and FeB are shown in Fig. S2† and can be indexed to COD data of 9008945 and 9008944, respectively.[23] The diffraction peaks show that the boride catalysts are crystalline. The PXRD patterns of the composite photoanodes reveal only the
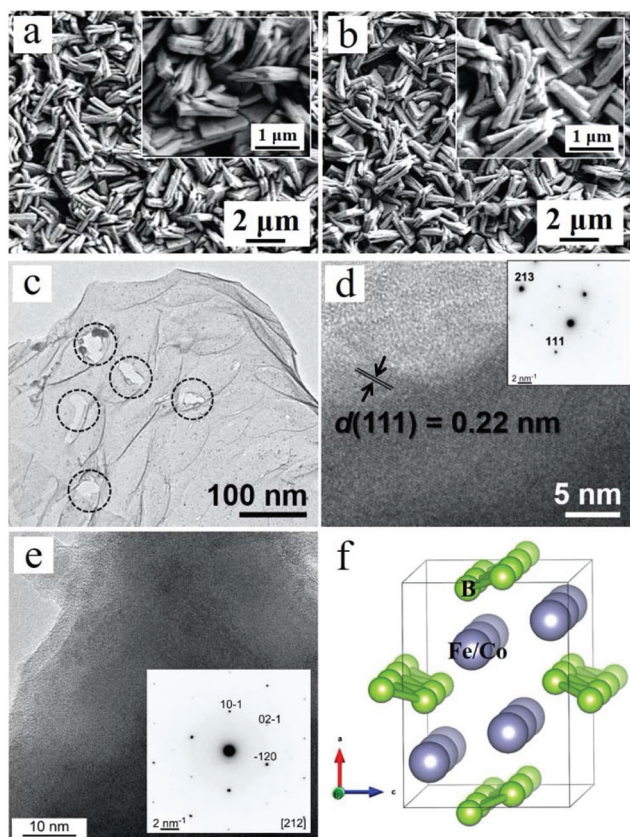
Fig. 1 SEM images of (a) WO₃/CoB and (b) WO₃/FeB. (c) TEM image of pristine CoB. The circles highlight defects in the two-dimensional structure. HRTEM images of CoB (d) and FeB (e) (insets: corresponding SAED patterns). (f) Crystal structure of CoB and FeB.

diffraction peaks stemming from the oxidic light absorber, because the catalyst loading was very small (*vide infra*). Fig. S3† shows the SEM images of bare WO₃ film. The film is composed of numerous porous WO₃ plates which are nearly perpendicularly aligned to the FTO substrate. Closer inspection reveals each plate to be composed of several primary units of thin WO₃ sheets with an average thickness of approximately 180 nm, showing a distinct sandwich-like structure. Representative SEM images of the bare CoB and FeB can be seen in our previous work.[23] The CoB is in the form of two-dimensional (2D) nanosheets while the FeB exhibits the feature of nanoplates.

Fig. 1a and b show the SEM images of the WO₃/CoB and WO₃/FeB, respectively. The morphological characteristics remain unaltered after the surface functionalization with MB catalysts, which can be attributed to the low loading content on the surface. The HRTEM images and corresponding SAED patterns confirm the high crystallinity of the bare CoB and FeB catalysts (Fig. 1c–e). Fig. 1f illustrates the corresponding crystal structure of orthorhombic CoB and FeB.

Photoelectrochemistry

The PEC water oxidation was investigated for bare WO₃, WO₃/CoB and WO₃/FeB photoanodes in 0.1 M Na₂SO₄ electrolyte
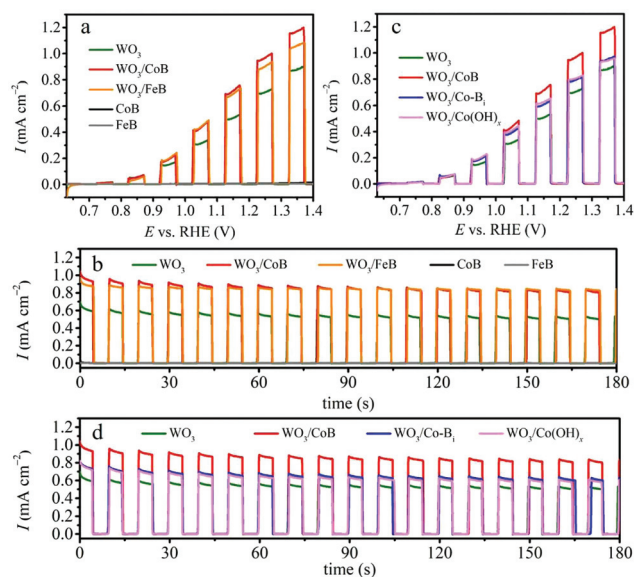
Fig. 2 (a) LSV and (b) CA curves of WO₃, WO₃/CoB and WO₃/FeB photoanodes. (c) LSV and (d) CA curves of WO₃, WO₃/CoB, WO₃/Co-Bᵢ and WO₃/Co(OH)ₓ photoanodes. All curves were recorded under interrupted AM 1.5G illumination in 0.1 M Na₂SO₄ electrolyte (pH 7).

(adjusted to pH 7) under interrupted illumination and optimized catalyst loading amount. LSV and CA at 1.23 V_RHE are shown in Fig. 2a and b. The complementary PEC water oxidation under constant illumination and optimization of catalyst loading amount are shown Fig. S4, S5 and S6,† respectively. All photoanodes do not exhibit dark current during the LSV, suggesting as such no occurrence of electrochemical reactions in the absence of illumination (Fig. S4†). All photoelectrodes develop an anodic photocurrent under simulated AM 1.5G light illumination. The UV-vis absorption edge of the as-prepared WO₃ thin film approaches *ca.* 460 nm (Fig. S7†), being equivalent to a band gap of 2.75 eV (*vide infra*). Even so, the pristine WO₃ photoanode exhibits an onset potential of *ca.* 0.7 V_RHE and a photocurrent density of 0.70 mA cm⁻² at 1.23 V_RHE (Fig. 2). This hints toward severe recombination of photogenerated charge carriers.

Upon the loading of CoB and FeB catalysts, a substantial upsurge of the photocurrent density to 0.95 and 0.89 mA cm⁻² *vs.* 1.23 V_RHE can be observed, respectively (Fig. 2a). Since the bare CoB and FeB produce negligible current during the LSV, the enhancement of photocurrent for the composite photoanodes stems synergistic effects between the WO₃ and MB catalysts. The onset potentials of pristine WO₃ and modified photoanodes are all close of 0.7 V_RHE; indicating that the conduction band edge, *i.e.* approximately the flat band potential, remains pinned after surface modification.[28,29] This result differs from the previously reported Fe₂O₃/FeB heterojunction photoanode,[21] where the onset potential exhibited a cathodic shift by about 80 mV in comparison to pristine Fe₂O₃. This difference suggests that the surface modification of above-mentioned MB catalysts highly depends on the substrate materials, coating methods and also surface coverage

achieved.[29] Transient CA at 1.23 V_{RHE} under interrupted illumination displays more obviously that surface modification of CoB and FeB meaningfully ameliorates the photocurrent density of WO_3 photoanode from 0.53 to 0.83 and 0.85 mA cm^{-2} (Fig. 2b, at 175 s), corresponding to a 1.57 times and 1.60 times enhancement, respectively. More importantly, the photocurrent decay of WO_3/FeB photoanode is effectively mitigated relative to the pristine one, demonstrating that the loading of the FeB catalyst can reduce the hole accumulation by accelerating the oxidation of H_2O to O_2.[28-30]

To give further perspective on our MB catalysts, the performance of CoB was compared against Co-B$_i$ and Co(OH)$_x$, with optimized amounts (Fig. S8 and S9†) under the same conditions (Fig. 2c and d). Complementary PXRD patterns for synthesized Co-B$_i$ and Co(OH)$_x$ catalysts are depicted in Fig. S8a and S9a†. Both compounds were revealed to be efficient OER catalysts possessing the potentials to reduce the overpotential and accelerate the OER kinetics.[31-34] Upon the loading of Co-B$_i$ and Co(OH)$_x$, the photocurrent enhances in comparison to the bare WO_3 photoanode, whereas a more considerable upsurge evolves for the CoB modified photoanode. This implies that the as-obtained CoB by the Sn/SnCl$_2$ solid-state method is more active than the other two cobalt species under these conditions. Furthermore, electrocatalytic water oxidation on bare CoB and Co-B$_i$ electrodes showed that higher current density could be obtained for the CoB catalyst (Fig. S10†). Interestingly, a related report also demonstrated a similar result for a nickel boride catalyst. Coupling the latter to $BiVO_4$ thin films surpasses the achieved photocurrent of an $BiVO_4$/Ni-B$_i$ photoanode.[20]

Generally, the surface modification can influence the PEC OER of WO_3 photoanodes in many ways, including: (i) the photoabsorption properties, and (ii) the separation efficiency of photogenerated charge carrier.[29] The SEM analysis showed that the morphological features of MB modified WO_3 thin films resemble the pristine one. On this basis, photoabsorption properties of the three photoanodes were investigated through UV-vis absorption spectroscopy (Fig. S7†). The photoabsorption edges of the three photoanodes are similar, at around 460 nm, whereas the photoabsorption intensity slightly diminishes from the wavelength of 300 to 430 nm. It implies that the photoabsorption difference by MB modification can be ruled out for the augmented photocurrent. The band gap of as-obtained WO_3 film is evaluated from the Kubelka–Munk-transformed reflectance spectrum to be 2.75 eV (Fig. 3a). Additionally, the flat band potential (E_F) is deduced to be 0.49 V_{RHE} for WO_3, based on the intersection in Mott–Schottky plot (Fig. 3b). The bottom of the conduction band (CB) for an n-type semiconductor is generally considered to be approximately 0.2 V more negative than E_F;[35] the CB value (E_{CB}) thus is estimated to be 0.29 V_{RHE}. Based on the determined electronic band gap, the band edge positions are visually presented as the inset in Fig. 3b, supporting its applicability to actuate water oxidation.

Prolonged CA manifests the amended stability of the photoanode coupling with FeB (Fig. S11†). The slight photocurrent
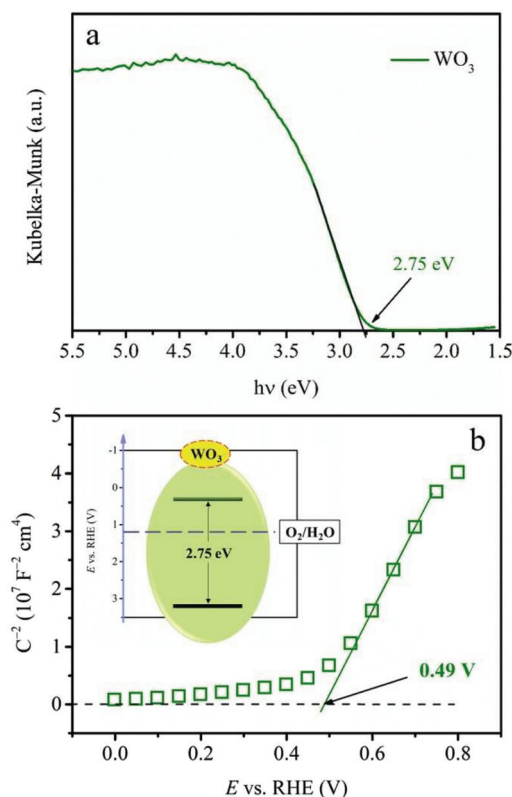

Fig. 3 (a) Band gap determined from the Kubelka–Munk-transformed reflectance spectrum. (b) Mott–Schottky plot of WO_3 film recorded at 10 Hz frequency under AM 1.5G illumination (insert: schematic of the energy levels of WO_3 film).

fading after MB modification can be attributed to the low surface coverage by the MB catalysts due to their small loading content.[36] This is also disclosed by the alike curvature between pristine WO_3 and WO_3/CoB photoanodes. We anticipate the surface modification of MB is accessible to passivate the WO_3 surface states by accelerating photoexcited carrier separation and migration, thus enhancing the OER activity.[37]

To verify this hypothesis, the charge carrier transport efficiency relevant to the bulk (η_{bulk}) and efficiency correlated to the surface trapping states ($\eta_{surface}$) are quantified by introducing Na_2SO_3 as hole scavenger.[28] The η_{bulk} and $\eta_{surface}$ can be calculated based on following equations:[38]

$$\eta_{bulk} = J_{sulphite}/J_{absorbed} \qquad (1)$$

$$\eta_{surface} = J/J_{sulphite} \qquad (2)$$

where J and $J_{sulphite}$ are photocurrent densities acquired in electrolyte without and with Na_2SO_3 (Fig. 4a and b), respectively, $J_{absorbed}$ correlates to photoabsorption expressed as a current density. Assuming the complete absorption and utilization of band gap photos of WO_3, a $J_{absorbed}$ value of 4 mA cm^{-2} is theoretically possible under AM 1.5G illumination.[39] Therefore, corresponding quantified contribution of MB on η_{bulk} and $\eta_{surface}$ are given in Fig. 4c and d. Apparently, surface functionalization with MB leads to a percentual increase in
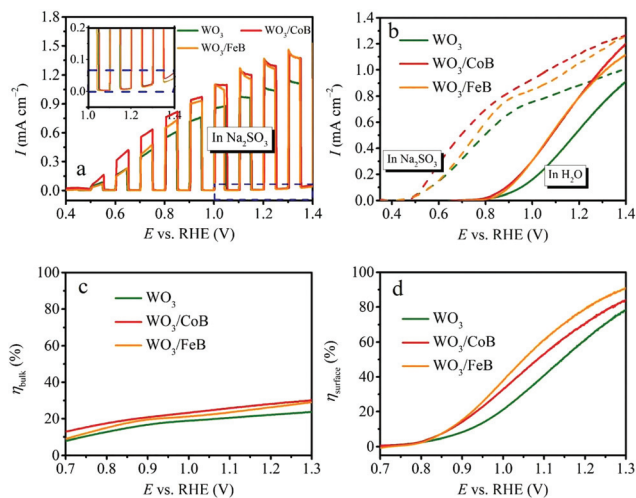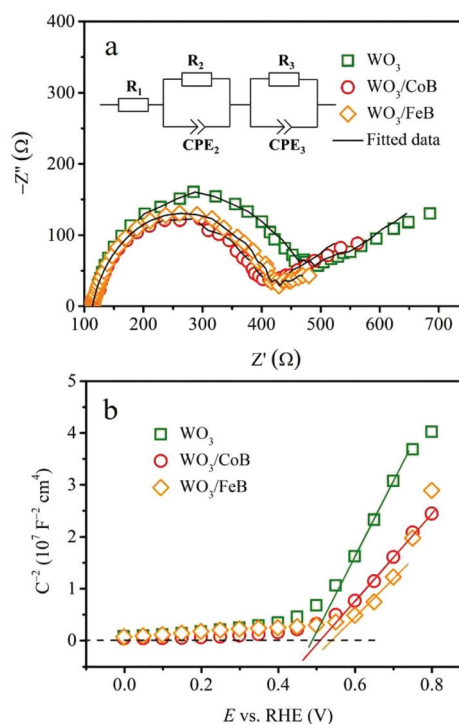
Fig. 4 LSV curves of WO_3, WO_3/CoB and WO_3/FeB photoanodes (a) recorded under interrupted AM 1.5G illumination in 0.1 M Na_2SO_4 containing 50 mM Na_2SO_3 (pH 7) (inset: partially enlarged area in (a)), (b) recorded under AM 1.5G illumination in 0.1 M Na_2SO_4 with (dashed lines) or without (solid lines) 50 mM Na_2SO_3 (pH 7, the current presented here is net photocurrent by deducting corresponding dark current). Charge separation efficiency (c) in the bulk and (d) on the surface of all photoanodes.

$\eta_{surface}$, whereas the promotion on η_{bulk} is relatively small. This manifests in improved PEC water oxidation and mainly stems from the mitigated carrier recombination on the surface.

To confirm the promoted charge carrier separation upon MB loading, a comparison of EIS data using Nyquist plots under AM 1.5G illumination were performed (Fig. 5a). The semicircles observed in the high frequency region represent the charge transport resistance in the bulk (R_2), whereas the others emerging in low frequency region reflect the charge transfer resistance at the electrode/electrolyte interface (R_3).[25,37] Additionally, the R_1 simulates the series resistance. The quantified results are exhibited in Table S1,† where the photoanodes coupling with MB catalysts display remarkable decrease of R_3 by almost half, if compared to the pristine one. It demonstrates that surface functionalization with MB catalysts improves hole extraction from the bulk and mitigates surface trapping. The WO_3 photoanode functionalized with CoB shows drastically decreased R_3, if compared to the Co-B$_i$ and Co(OH)$_x$ (Fig. S12 and Table S2†). It should be noted that the slightly higher photocurrent for WO_3 electrodes which were modified with Co-B$_i$ in comparison to Co(OH)$_x$ is reflected in the smaller R_3 value for WO_3/Co-B$_i$. Bode phase plots are presented in Fig. S13† to further elucidate the effect of MB loading on holes in transfer ability, lifetime and recombination.[40,41] With respect to the pristine WO_3 photoanode (24.76 ms), the CoB- and FeB-decorated photoanodes possess prolonged holes lifetime of 26.8 and 32.3 ms, respectively.

Mott–Schottky investigation based on capacitances derived from the electrochemical impedance were carried out at 10 Hz frequency under AM 1.5G illumination. Since the slopes of the

Fig. 5 (a) EIS Nyquist plots with fitted curves at a bias of 1 V_{RHE} (insert: the equivalent circuit model). (b) Electrochemical Mott−Schottky plots of WO_3, WO_3/CoB and WO_3/FeB photoanodes at frequency of 10 Hz, recorded in 0.1 M Na_2SO_4 electrolyte (pH 7) under AM 1.5G illumination.

curves are inversely proportional to the charge carrier density,[42] the introduction of MB catalysts is responsible for the increase of charge carrier density (Fig. 5b). Compared with pristine WO_3 photoanode, the photogenerated holes in MB modified photoanode-driven system possess prolonged lifetime, increased density and corrected transport efficiency. Consequently, the PEC water oxidation activity and stability of WO_3 photoanodes are increased. The MS-plot for the CoB-modified photoanode exhibits also a smaller slope in comparison to WO_3 electrodes that have been modified with Co-B$_i$ and Co(OH)$_x$ (Fig. S14†).

Open circuit photovoltage and surface band bending

The open circuit voltage (OCV) decay measurements were conducted in dark and upon AM 1.5G illumination in Ar atmosphere (Fig. 6a). The open circuit photovoltage (OCP) = OCV in light (OCV$_{light}$) − OCV in dark (OCV$_{dark}$), represents the band bending degree.[20,43] A space-charge layer (SCL) at the electrode/electrolyte interface can spontaneously form by immersing the electrode into the electrolyte, due to the equilibration of the WO_3 Fermi-level (E_f) with the chemical potential of electrolyte (Fig. 6b).[44]

It has been demonstrated that an enlarged band bending at the SCL of WO_3, correlated with changes in surface states, is indicative of the facilitated separation of photoexcited electron–hole pairs and prolonged carrier lifetime.[43,44] In the OCV time profile (Fig. 6a), the OCP upraises from pristine WO_3 to
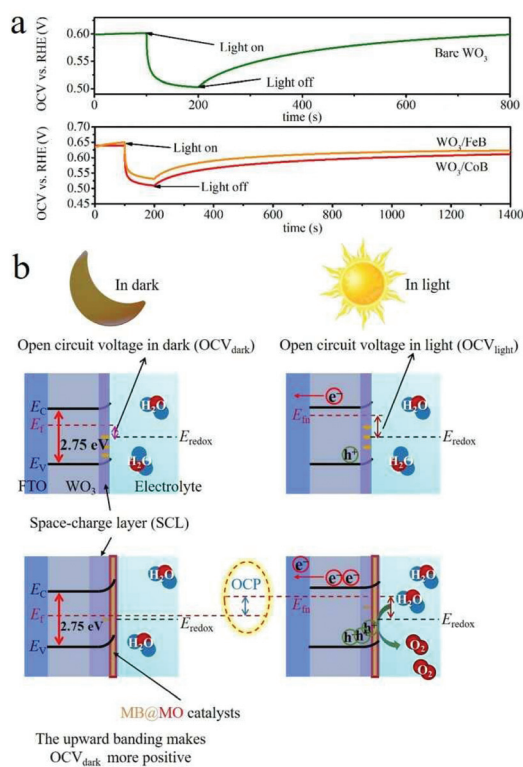
Fig. 6 (a) OCV time profile of pristine WO₃ and WO₃/MB photoanodes recorded in Ar atmosphere. (b) Band structures and band bending schematics of the WO₃ based photoanodes.

WO₃/MB photoanodes, which thus indicates the enlarged band bending and promoted charge carrier separation.

Fig. 6b schematically summarizes the band structures and band bending diagrams relative to OCV$_{dark}$ and OCV$_{light}$ values. As for WO₃ photoanode, the relative high OCV$_{dark}$ was achieved when it was immersed in solution, because of the Fermi-level pinning by surface trapped electrons (Fig. 6b).[4] It implies the upward band bending nature of the electrode in equilibrium with the electrolyte in dark.[43] In contrast, a moderate OCV$_{light}$ under illumination suggests the flattened band induced by photoexcited carrier.[43] By the introduction of MB catalysts, the E_f shifts more positively compared to pristine photoanode, due to the mitigated E_f pinning effect by passivating surface trapping states.[4] Therefore, a upgraded OCP value is achieved after coupling MB to WO₃ photoanodes.[4,43]

It is noteworthy that in the OCV measurements the catalytic and kinetic impacts can be excluded, because within the system the current originating from the hypothetic redox reactions does not pass steadily.[43] Meanwhile, the Ar atmosphere also prevented the measurements being interfered from the surface states passivation by dissolved-O₂ absorption.

Additionally, in Fig. 6a, the WO₃/MB exhibit much slow decay curves after terminating the illumination, specifically, their OCV have not been completely restored even after 1200 s. It further suggests a much longer charge carrier lifetime within the functionalized photoanodes in comparison with the pristine one.[45,46] Therefore, the enhanced band bending

correlated with changes in surface states is responsible for the prolonged holes lifetime and amended charge carrier recombination in MB modified photoanodes.

In situ formation of core–shell MB@MO catalysts

Since the surface composition and chemical state are crucial to the catalytic performance, XPS was employed to characterize the chemical states of a complementary bare CoB electrode after CA for 20 min. The B 1s high-resolution XP spectrum (Fig. 7a) shows one distinct peak at 191.7 eV corresponding to the photoemission from boron-oxo species, which dominate on the surface of the catalysts after OER, as described in some previous reports.[16,20,47] In turn, the Co 2p high-resolution XP spectrum (Fig. 7b) exhibits spin–orbit splitting with two components – Co 2p$_{3/2}$ at 780.8 eV and Co 2p$_{1/2}$ at 796.7 eV. The deconvolution of Co 2$_{p3/2}$ can be done by two peaks at 780.6 and 782.5 eV, which together with the intense satellite features at 785.6 and 789.6 eV manifest a predominant role of Co²⁺ in the oxide/hydroxide form.[16,43] Because of the very limited detection depth of XPS, the signals from elemental B and Co beneath the surface layer are hard to be detected here.[48] On the other hand, the identical forms of Co and B species (confirmed by the Co 2p and B 1s components appearing in the same binding energies) are found for the bare CoB electrode soaked in distilled water for 1 min and dried at 50 °C (Fig. S15†).

A representative STEM EELS spectrum (Fig. 7c) was extracted from the edge of the sample. The data were acquired in spectrum imaging mode, which allows us to separate the edge contributions from the bulk. The EELS spectrum in
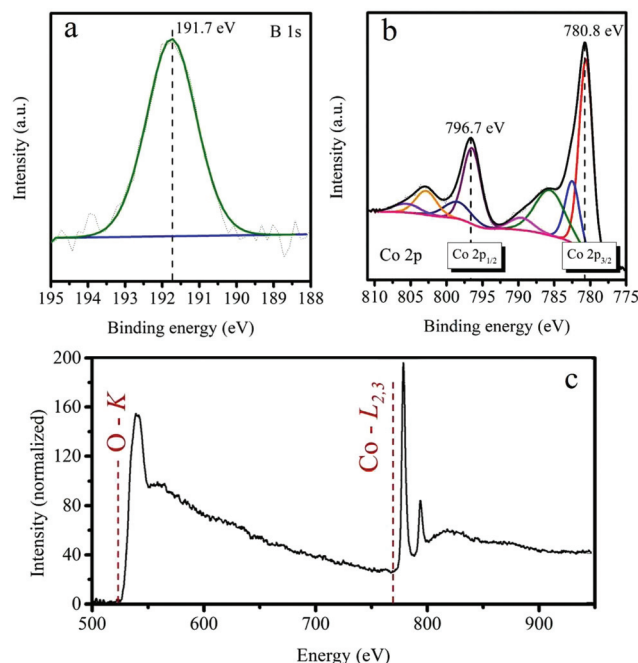
Fig. 7 XPS core level analyses of (a) B 1s, (b) Co 2p. (c) STEM EELS spectrum of CoB electrode. All data were recorded on a CoB electrode that has been subject to CA at 1.23 V$_{RHE}$ under illumination.
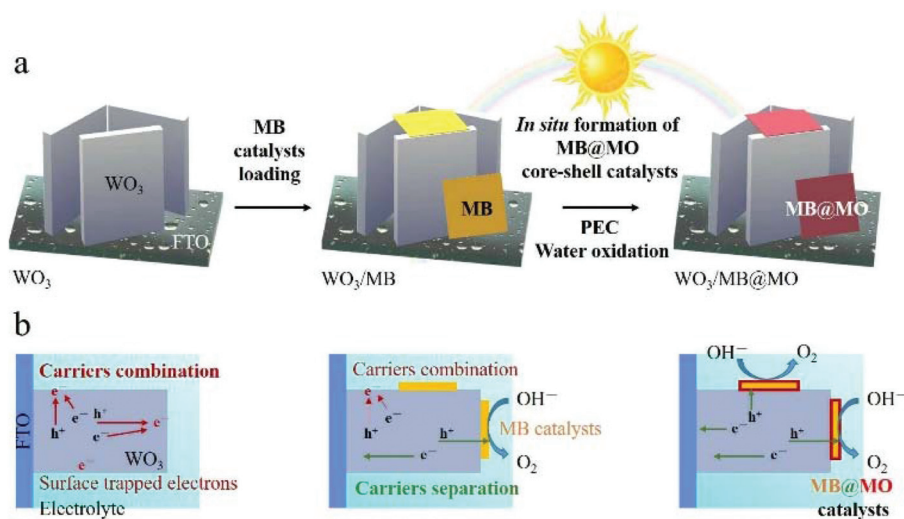
Fig. 8 (a) Fabrication of the FTO/WO$_3$/MB@MO photoanodes, including (1) synthesis of WO$_3$ thin film on FTO, (2) surface modification with MB catalysts, (3) *in situ* formation of FTO/WO$_3$/MB@MO photoanodes during PEC measurement. (b) Photogenerated charge carrier recombination and separation processes in pristine WO$_3$, WO$_3$/MB and WO$_3$/MB@MO photoanodes.

Fig. 7c has been deconvoluted with the low-loss EELS spectrum. The Energy-Loss Near-Edge Structure (ELNES) fingerprint on the resulting spectral shape is very similar to CoO.

In combination with XPS, these results imply the existence of a CoO$_x$-rich layer, being demonstrated as one of the active species.[49] The shell is formed *in situ* on the surface of the catalyst during PEC water oxidation. The active form of the catalyst is thus inferred to consist of a MB core wrapped by a MO-rich layer, and is represented as MB@MO (Fig. 7 and 8). Similar layers on the surface of core–shell like catalysts had also been revealed to be responsible for promoted OER.[50,51]

Fig. 8a summarizes the structural evolution steps for the WO$_3$/MB@MO photoanodes and the corresponding scheme for accelerated charge carrier migration is shown in Fig. 8b.

Conclusions

In summary, we have integrated crystalline CoB and FeB nanostructures as catalysts with WO$_3$ photoanodes for PEC water oxidation for the first time. The modification of the WO$_3$ surface enables a *ca.* 1.6-fold upsurge of the photocurrent and improves its stability. The WO$_3$ photoanodes functionalized with CoB also surpass the PEC performance of WO$_3$/Co-B$_i$ and WO$_3$/Co(OH)$_x$ photoanodes. Kinetic analysis demonstrates that the enlarged band bending, correlated with the passivation of surface states which inhibits recombination, is responsible for the augmented charge carrier separation in heterojunction electrodes. The *in situ* reconstructed catalyst surface MB@MO is the active catalytic center for the water oxidation. The present study highlights the significance of interface interactions within heterojunction systems for future development of photoelectrodes.

Conflicts of interest

There are no conflicts to declare.

Acknowledgements

Notes and references

1 T. Hisatomi and K. Domen, *Nat. Catal.*, 2019, **2**, 387–399.
2 G. Glenk and S. Reichelstein, *Nat. Energy*, 2019, **4**, 216–222.
3 J. M. V. Nsanzimana, R. Dangol, V. Reddu, S. Duo, Y. Peng, K. N. Dinh, Z. Huang, Q. Yan and X. Wang, *ACS Appl. Mater. Interfaces*, 2019, **11**, 846–855.
4 K.-H. Ye, H. Li, D. Huang, S. Xiao, W. Qiu, M. Li, Y. Hu, W. Mai, H. Ji and S. Yang, *Nat. Commun.*, 2019, **10**, 3687.
5 T. Higashi, H. Nishiyama, Y. Suzuki, Y. Sasaki, T. Hisatomi, M. Katayama, T. Minegishi, K. Seki, T. Yamada and K. Domen, *Angew. Chem., Int. Ed.*, 2019, **58**, 2300–2304.

6 S. Vanka, E. Arca, S. Cheng, K. Sun, G. A. Botton, G. Teeter and Z. Mi, *Nano Lett.*, 2018, **18**, 6530–6537.

7 K. Choi, K. Kim, I. K. Moon, J. Bang and J. Oh, *Nanoscale*, 2019, **11**, 15367–15373.

8 M. Davi, A. Drichel, M. Mann, T. Scholz, F. Schrader, A. Rokicinska, P. Kustrowski, R. Dronskowski and A. Slabon, *J. Phys. Chem. C*, 2017, **121**, 26265–26274.

9 Z. Ma, T. Thersleff, A. L. Görne, N. Cordes, Y. Liu, S. Jakobi, A. Rokicinska, Z. G. Schichtl, R. H. Coridan, P. Kustrowski, W. Schnick, R. Dronskowski and A. Slabon, *ACS Appl. Mater. Interfaces*, 2019, **11**, 19077–19086.

10 R. Nebel, K. M. Macounová, H. Tarábková, L. Kavan and P. Krtil, *J. Phys. Chem. C*, 2019, **123**, 10857–10867.

11 D. K. Lee, D. Lee, M. A. Lumley and K.-S. Choi, *Chem. Soc. Rev.*, 2019, **48**, 2126–2157.

12 Z. Ma, O. Linnenberg, A. Rokicinska, P. Kustrowski and A. Slabon, *J. Phys. Chem. C*, 2018, **122**, 19281–19288.

13 M. Davi, G. Ogutu, F. Schrader, A. Rokicinska, P. Kustrowski and A. Slabon, *Eur. J. Inorg. Chem.*, 2017, **2017**, 4267–4274.

14 C. Ding, J. Shi, Z. Wang and C. Li, *ACS Catal.*, 2017, **7**, 675–688.

15 J. A. Seabold and K.-S. Choi, *J. Am. Chem. Soc.*, 2012, **134**, 2186–2192.

16 J. Masa, P. Weide, D. Peeters, I. Sinev, W. Xia, Z. Sun, C. Somsen, M. Muhler and W. Schuhmann, *Adv. Energy Mater.*, 2016, **6**, 1502313.

17 J. M. V. Nsanzimana, V. Reddu, Y. Peng, Z. Huang, C. Wang and X. Wang, *Chem. – Eur. J.*, 2018, **24**, 18502–18511.

18 J. Masa, I. Sinev, H. Mistry, E. Ventosa, M. de la Mata, J. Arbiol, M. Muhler, B. Roldan Cuenya and W. Schuhmann, *Adv. Energy Mater.*, 2017, **7**, 1700381.

19 W. Jiang, S. Niu, T. Tang, Q.-H. Zhang, X. Liu, Y. Zhang, Y.-Y. Chen, J.-H. Li, L. Gu, L.-J. Wan and J.-S. Hu, *Angew. Chem., Int. Ed.*, 2017, **56**, 6572–6577.

20 K. Dang, X. Chang, T. Wang and J. Gong, *Nanoscale*, 2017, **9**, 16133–16137.

21 A. Liao, H. He, Z. Fan, G. Xu, L. Li, J. Chen, Q. Han, X. Chen, Y. Zhou and Z. Zou, *J. Catal.*, 2017, **352**, 113–119.

22 H. Han, Y. Hong, J. Woo, S. Mhin, K. M. Kim, J. Kwon, H. Choi, Y. Chung and T. Song, *Adv. Energy Mater.*, 2019, **9**, 1803799.

23 P. R. Jothi, K. Yubuta and B. P. T. Fokwa, *Adv. Mater.*, 2018, **30**, 1704181.

24 H. Park, Y. Zhang, J. P. Scheifers, P. R. Jothi, A. Encinas and B. P. T. Fokwa, *J. Am. Chem. Soc.*, 2017, **139**, 12915–12918.

25 D. Hu, P. Diao, D. Xu and Q. Wu, *Nano Res.*, 2016, **9**, 1735–1751.

26 P. Chen, K. Xu, T. Zhou, Y. Tong, J. Wu, H. Cheng, X. Lu, H. Ding, C. Wu and Y. Xie, *Angew. Chem., Int. Ed.*, 2016, **55**, 2488–2492.

27 C. Zhen, L. Wang, G. Liu, G. Q. (Max) Lu and H. Cheng, *Chem. Commun.*, 2013, **49**, 3019–3021.

28 M. Yang, H. He, H. Zhang, X. Zhong, F. Dong, G. Ke, Y. Chen, J. Du and Y. Zhou, *Electrochim. Acta*, 2018, **283**, 871–881.

29 W. Kim, T. Tachikawa, D. Monllor-Satoca, H. Kim, T. Majima and W. Choi, *Energy Environ. Sci.*, 2013, **6**, 3732–3739.

30 J. Huang, Y. Zhang and Y. Ding, *ACS Catal.*, 2017, **7**, 1841–1845.

31 X. Ren, R. Ge, Y. Zhang, D. Liu, D. Wu, X. Sun, B. Du and Q. Wei, *J. Mater. Chem. A*, 2017, **5**, 7291–7294.

32 C. Xie, Y. Wang, D. Yan, L. Tao and S. Wang, *Nanoscale*, 2017, **9**, 16059–16065.

33 L. Wang, B. Zhang and Q. Rui, *ACS Catal.*, 2018, **8**, 10564–10572.

34 G. Zhang, S. Zang and X. Wang, *ACS Catal.*, 2015, **5**, 941–947.

35 B. Dong, J. Cui, Y. Gao, Y. Qi, F. Zhang and C. Li, *Adv. Mater.*, 2019, **31**, 1808185.

36 M. Ertl, Z. Ma, T. Thersleff, P. Lyu, S. Huettner, P. Nachtigall, J. Breu and A. Slabon, *Inorg. Chem.*, 2019, **58**, 9655–9662.

37 M. Ma, K. Zhang, P. Li, M. S. Jung, M. J. Jeong and J. H. Park, *Angew. Chem., Int. Ed.*, 2016, **55**, 11819–11823.

38 Y. Zhong, Z. Li, X. Zhao, T. Fang, H. Huang, Q. Qian, X. Chang, P. Wang, S. Yan, Z. Yu and Z. Zou, *Adv. Funct. Mater.*, 2016, **26**, 7156–7163.

39 S. Wang, H. Chen, G. Gao, T. Butburee, M. Lyu, S. Thaweesak, J.-H. Yun, A. Du, G. Liu and L. Wang, *Nano Energy*, 2016, **24**, 94–102.

40 L. Ma, H. Fan, M. Li, H. Tian, J. Fang and G. Dong, *J. Mater. Chem. A*, 2015, **3**, 22404–22412.

41 L. Ma, H. Fan, J. Wang, Y. Zhao, H. Tian and G. Dong, *Appl. Catal., B*, 2016, **190**, 93–102.

42 D. Kim, Z. Zhang and K. Yong, *Nanoscale*, 2018, **10**, 20256–20265.

43 M. Zhong, T. Hisatomi, Y. Kuang, J. Zhao, M. Liu, A. Iwase, Q. Jia, H. Nishiyama, T. Minegishi, M. Nakabayashi, N. Shibata, R. Niishiro, C. Katayama, H. Shibano, M. Katayama, A. Kudo, T. Yamada and K. Domen, *J. Am. Chem. Soc.*, 2015, **137**, 5053–5060.

44 S. Corby, E. Pastor, Y. Dong, X. Zheng, L. Francàs, M. Sachs, S. Selim, A. Kafizas, A. A. Bakulin and J. R. Durrant, *J. Phys. Chem. Lett.*, 2019, **10**, 5395–5401.

45 Y. Wang, S. Jin, G. Pan, Z. Li, L. Chen, G. Liu and X. Xu, *J. Mater. Chem. A*, 2019, **7**, 5702–5711.

46 Y. Wang, S. Jin, X. Sun, S. Wei, L. Chen and X. Xu, *Appl. Catal., B*, 2019, **245**, 10–19.

47 T. Tan, P. Han, H. Cong, G. Cheng and W. Luo, *ACS Sustainable Chem. Eng.*, 2019, **7**, 5620–5625.

48 L.-K. Wu, W. Wu, J. Xia, H. Cao, G. Hou, Y. Tang and G. Zheng, *Electrochim. Acta*, 2017, **254**, 337–347.

49 D. Li, J. Shi and C. Li, *Small*, 2018, **14**, 1704179.

50 L.-A. Stern, L. Feng, F. Song and X. Hu, *Energy Environ. Sci.*, 2015, **8**, 2347–2351.

51 N. T. Suen, S. F. Hung, Q. Quan, N. Zhang, Y. J. Xu and H. M. Chen, *Chem. Soc. Rev.*, 2017, **46**, 337–365.